

Direct Thermal Polymerization Approach to N-Rich Holey Carbon Nitride Nanosheets and Their Promising Photocatalytic H₂ Evolution and Charge-Storage Activities

Bindu Antil,[†] Lakshya Kumar,[†] K. P. Reddy,[‡] C. S. Gopinath,[‡]^{ID} and Sasanka Deka*,[†]^{ID}

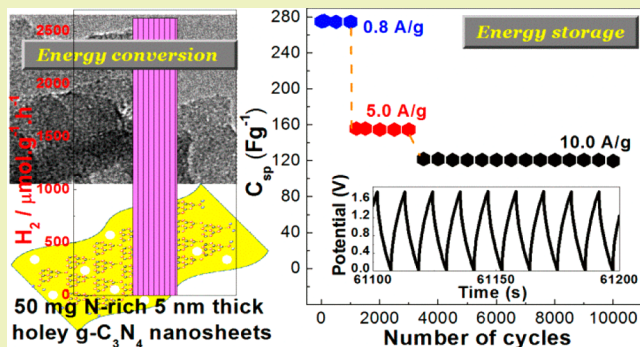
[†]Department of Chemistry, University of Delhi, North Campus, Delhi 110007, India

[‡]Catalysis Division, National Chemical Laboratory, Dr. Homi Bhabha Road, Pune 411 008, India

Supporting Information

ABSTRACT: Energy conversion and energy storage are two crucial challenges in green chemistry that have attracted tremendous attention for the last several decades. In this work, we have addressed both issues by synthesizing nitrogen-rich, few-layer-thick holey graphitic carbon nitride ($\text{g-C}_3\text{N}_4$) nanosheets by a simple, novel, direct thermal polymerization method, which is found to be very good in photocatalytic H₂ evolution reaction (energy-conversion) and charge-storage supercapacitor (energy-storage) applications. This as-synthesized conjugated polymer semiconductor (obtained stoichiometry $\text{C}_3\text{N}_{4.8}$) with unique structural and morphological advantages exhibits superior photocatalytic water splitting activity to H₂ evolution ($2.620 \mu\text{mol h}^{-1} \text{ g}^{-1}$) without the help of any cocatalysts under visible light in the presence of 20% triethanolamine (TEOA). The calculated apparent quantum yield is 8.5% at 427 nm, and the rate of photocatalytic hydrogen generation remained constant for nine consecutive catalytic cycles (9 h photocatalysis). The present material also shows electrochemical double layer capacitor (EDLC) behavior in alkaline electrolyte, where a symmetric coin cell device consisting of this electrode material without any large area support or conductive filler delivers high specific capacitance (275 F g^{-1}), energy density (30 Wh kg^{-1}), and power density (6651 W kg^{-1}), and the supercapacitor cell can retain >98% capacitance efficiency up to 10 000 measured cycles at various current densities.

KEYWORDS: $\text{g-C}_3\text{N}_4$, Nanosheets, Photocatalyst, Supercapacitor, Water splitting, Hydrogen evolution



INTRODUCTION

Graphitic carbon nitride is a two-dimensional conjugated polymer and as a family of carbon nitride compounds has drawn broad interdisciplinary attention due to its metal-free semiconducting nature and potential photocatalytic and electrical activities. It also offers properties like high hardness, chemical robustness, high mechanical and chemical stability, etc. Because of its optimum bulk band gap energy (~2.7 eV), high visible-light absorption coefficient, and environmentally friendly nature, it has been studied extensively as a catalyst in photocatalytic and electrochemical water splitting.^{1–7} The properties of carbon nitrides depend mainly on parameters such as structure, composition, and crystallinity. It is found that carbon nitride exists in five different structures, viz., one 2D $\text{g-C}_3\text{N}_4$, four 3D $\alpha\text{-C}_3\text{N}_4$, $\beta\text{-C}_3\text{N}_4$, cubic- C_3N_4 , and pseudocubic C_3N_4 .⁸ Among all of these structures, $\text{g-C}_3\text{N}_4$ is observed as a chemically and thermally stable layered material analogous to graphite with versatile electronic properties. It is named $\text{g-C}_3\text{N}_4$ because its structure is similar to graphitic nanostructure.⁹ This low-cost, metal-free semiconductor can be easily prepared under mild conditions using cheap feedstocks like urea, cyanamide, thiourea, melamine, etc.

Because of its versatile properties, it has been studied in a wide range of applications such as capturing CO₂, reduction of CO₂, storage of hydrogen, water purification and sensing of toxic molecules, photodegradation of organic pollutants, and dehydrogenation reaction, apart from popular visible-light-driven photocatalytic hydrogen generation from water.^{10–18} Hydrogen production by a renewable green method from water is in priority globally as H₂ is considered to be the most important, cleanest energy fuel in the near future with high energy capacity, environmentally benign quality, and good recyclability performance.^{8,19} Unfortunately, the photocatalytic performance of $\text{g-C}_3\text{N}_4$ is still restricted by its low specific surface area, fast recombination of photoinduced electron–hole pairs, and narrow light absorption range.^{20,21} To overcome these disadvantages, there are several literature reports that point out methods to develop $\text{g-C}_3\text{N}_4$ nanostructures and focus on enhancing the photocatalytic activity of $\text{g-C}_3\text{N}_4$ for hydrogen evolution by introducing a noble metal

Received: January 30, 2019

Revised: April 4, 2019

Published: April 17, 2019

cocatalyst (usually expensive) that acts as a sink for photogenerated electrons and prevents exciton recombination and also the increase in surface area. Among the published reports, maximum H₂ evolution is observed when Pt or Au nanoparticles were used as cocatalysts (hybrid nanoparticle) or H₂PtCl₆·6H₂O was added during the water splitting reaction.^{21–28} The various synthetic methods in recent reports mainly focus on the construction of two-dimensional porous nanostructures because of the advantages such as the following: (a) the two-dimensional (2D) feature results in high charge separation and transportability and (b) the porous structure leads to high surface area, which, as a result, enhances the photocatalytic activity. Generally, the porous structure of g-CN is achieved using expensive hard templates or some hazardous chemicals. Also the hard templates used to get the pores are finally removed using hazardous chemicals, which again harms the environment and creates pollution.¹⁰

Because g-C₃N₄ can be prepared in 2D nanosheet (NS) morphology and it is analogous to graphene, there is interest in whether it can be used as an energy-storage materials as well, such as a supercapacitor possessing electric double layer capacitive (EDLC) behavior.^{29–32} An EDLC-type supercapacitor, a class of energy-storage devices, employs a double layer of charged particles (without dielectric) formed on activated carbon material electrodes in an electrolyte that are usable in applications that need a high capacitance in a thin package.^{33,34} However, performances of all carbonaceous materials are not very good as capacitor due to their low specific energy and inert surface. The existence of nitrogen in carbonaceous materials improves capacity while maintaining excellent cyclability of supercapacitors, and it enhances the wettability and in consequence improves efficient utilization of the surface. Therefore, g-C₃N₄ could be a new alternative to a few popular carbonaceous materials as it possesses higher concentration of nitrogen that is favorable for higher conductivity and electrochemical performance.^{21,35} At the same time, a 2D structure with high surface area will provide a large electrode–electrolyte contact area.³⁰

Therefore, it would be interesting and promising if one can prepare a metal-free, highly porous 2D g-C₃N₄ nanostructure with additional nitrogen atoms. The synergistic effect due to free lone pairs of electrons at the additional N atoms bonded at the surface of g-C₃N₄ planar structure and g-C₃N₄ nanostructure is expected to enhance conductivity as well as catalytic sites.^{21,36} Here, in this report we have used a simple and novel direct thermal polymerization approach to synthesize ~5 nm thick holey g-C₃N₄ nanosheets without the use of any hard templates. Direct heating of melamine with ammonium carbonate formed highly porous N-rich g-C₃N_{4.8} (NCN) stoichiometric nanostructure due to the decomposition of ammonium carbonate, which is further exfoliated using mild acid treatment to form few-layered ultrathin NCN nanosheets. Benefiting from the two-dimensional porous sheetlike structure, this NCN without any kind of cocatalyst (including the added H₂PtCl₆·6H₂O solution) exhibits excellent photocatalytic H₂ production activity under visible-light irradiation with a prominent apparent quantum yield, which is stable for continuous 9 h consecutive cycles. Furthermore, the present material shows electrochemical charge-storage (EDLC) behavior in alkaline electrolyte in such a manner that it can be used as a replacement of reduced-graphene oxide (RGO) if required. It also revealed a good rate capability without the use of Ni-foam substrate. The efficiency of our g-C₃N₄ NS

electrode-based cell remains >98% stable up to measured 10 000 galvanostatic charge–discharge cycles.

EXPERIMENTAL SECTION

Synthesis of N-Rich Holey Carbon Nitride Nanosheets. A novel and simple direct thermal polymerization approach has been used for the synthesis of N-rich holey carbon nitride NSs. In a typical synthesis, equal amounts of melamine (2 g) and ammonium carbonate (2 g) were mixed in an alumina crucible, and the crucible was covered with a lid and put into a muffle furnace. The mixture was then heated in air at 550 °C with a heating rate of 2 °C min⁻¹ for 5 h for polymerization. A yellow color product was formed that was then crushed to a fine powder using mortar and pestle. The fine powder was then transferred to a beaker, 25 mL of 3 M HCl was added to it, and the mixture was stirred for 12 h. The obtained yellow product was centrifuged and washed with water three times, finally dried at 60 °C overnight, and reserved for further studies. The bulk sample (BCN) was synthesized by simply heating the melamine at 550 °C for 5 h, and it was further used for comparison of activity with g-C₃N₄ NS sample.

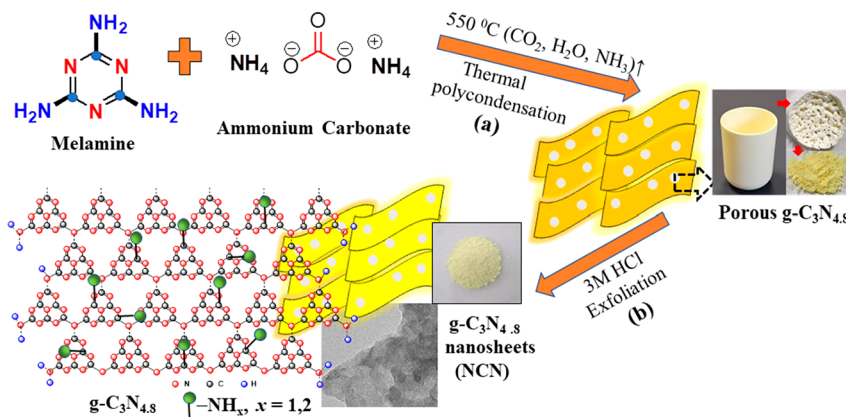
Photocatalytic Measurements. Photocatalytic H₂ evolution reaction was conducted in a 50 mL airtight quartz reactor connected to a circulating cooling water system.³⁷ The temperature of circulating water has been maintained constant throughout the photocatalytic reaction by using a chiller. The reactor has been connected to an inverted buret to calculate the amount of gas evolved during the reaction. All the reactions have been done under visible-light irradiation that uses a 250 W mercury lamp as the visible-light source (Philips Standard bulb HPL-N 250W E40 200–250 V mercury vapor lamp), which is equipped with an UV-cut off filter to obtain visible light. For each test, 50 mg of the finely ground powder photocatalyst was dispersed in an aqueous solution of 50 mL of 20% triethanolamine by volume. The reaction has been performed using both NCN and bulk C₃N₄ photocatalysts. Before each photocatalytic test, the closed system was degassed by N₂ for 0.5 h to drive away O₂. The hydrogen evolved during the reaction has been detected using an online gas chromatograph GC-7890B (Agilent Technologies) instrument with thermal conductivity detector (TCD) and high-purity He as the carrier gas. The distance between the light source and the reaction mixture was 12 cm, the average intensity of the mercury bulb determined by an auto digital luxmeter MTQ 1010A was found to be 0.00768 W/cm², and the measured area of irradiation was 31.41 cm². The apparent quantum efficiency (AQE) for hydrogen evolution at different wavelengths was calculated using the following equation,^{23,38}

$$\text{AQE} = \frac{2n\text{H}_2}{\text{number of incident photons}} \times 100 (\%) \quad (1)$$

where nH₂ is the number of H₂ molecules produced per second.

Charge-Storage Measurements. The electrochemical charge-storage behaviors of our samples were first examined using a three-electrode system in 1.0 M KOH aqueous solution. Initially the working electrodes (Cell#NCN, Cell#BCN) were prepared by mixing 10:10:80 of acetylene carbon/PVDF/active material in acetone to obtain well-sonicated, dispersed, viscous slurry, which was then further deposited over a graphite sheet of ~250 μm thickness using the spin-coating technique. The prepared electrode was finally dried at 50 °C for 12 h. To calculate the weight of deposited electrode material (0.6 mg) over graphite sheet (1 cm²), weighing of the graphite sheet was done before and after deposition of the electrode material. During the measurements, Ag/AgCl was used as a reference electrode and a platinum sheet (1 cm²) was used as the counter electrode. Second, a coin cell testing device was assembled because it mimics the physical configuration, internal voltages, and charge transfer that occur in a real supercapacitor cell and thereby provides the best indication of an electrode material's device performance. For this, 100 mg of the NCN sample was dispersed in 3 mL of isopropyl alcohol (IPA) by sonicating it for 30 min, and the slurry was smeared onto graphite sheets (1 cm² × 1 cm²). The weight of the deposited electrode material was 1.0 mg/cm². A coin cell assembly (CR-2032)

Scheme 1. Sketch of the Synthetic Procedure Devised to Synthesize Few-Layered N-Rich Holey g-Carbon Nitride Nanosheets in This Work



was fabricated by putting a negative case, spring, spacer, cathode, separator, anode, and positive case in their respective orders, and finally the coin cell assembly was punched using a punching machine. A symmetrical configuration supercapacitor was achieved where Whatman glass microfiber filters (GF/C) soaked in electrolyte (6.0 M KOH) act as a separator that is finally sandwiched between two symmetric electrodes. To study the electrochemical properties, cyclic voltammetry (CV), galvanostatic charge–discharge (GCD) analysis, and electrochemical impedance spectroscopy (EIS) were performed on a CHI 660E (U.S.A.) electrochemical workstation. The discharge-specific capacitance (C_{sp}) was determined from the slope of the discharge characteristic curve using the following expressions,^{39,40}

$$C_{sp} = i \times \Delta t / m \Delta V \quad (2)$$

$$C_{sp} = 2 \times (i \times \Delta t / m \Delta V) \quad (3)$$

where i is the constant loaded current, ΔV is the potential window during discharge, Δt is the discharge time, and m is the mass of single electrode material without a current collector. Equations 2 and 3 are used for three-electrode and two-electrode (coin cell) configurations, respectively. The energy density (E) and power density (P) parameters are calculated using the following expressions,^{39,40}

$$E = \frac{1}{2M} CV^2 \quad (4)$$

$$P = \frac{V^2}{4M \times ESR} \quad (5)$$

where M is the total mass loading and $ESR = iR_{drop}/2I$. Here iR_{drop} is the sudden potential drop during the discharge process.

RESULTS AND DISCUSSION

A direct polymerization and exfoliation-mediated two-step green and simple synthesis strategy has been developed to synthesize ultrathin graphitic-C₃N₄ nanosheets. A schematic diagram of the synthesis approach to obtain few-nanometer-thick holey g-C₃N₄ nanosheets is shown in Scheme 1. A reaction between melamine and ammonium carbonate at 550 °C in air atmosphere in step (a) produces yellowish graphitic C₃N₄ nanostructures that become highly porous in nature due to the decomposition of ammonium carbonate (and consequently evaporation of CO₂, NH₃, and H₂O) during the heating process. However, these nanostructures are not thin enough to be termed as nanosheets (Figure S1). To make them few-nanometer-thick nanosheets, a liquid-phase exfoliation process was followed. In the liquid-phase exfoliation process in step (b) of Scheme 1, ultrathin holey NCN NSs (~5 nm thick) were produced just by stirring the as-produced g-

C₃N₄ in 3 M HCl without any long-time sonication process as followed previously.⁴¹ Presence of (NH₄)₂CO₃ during the polymerization process helps the final product g-C₃N₄ to be N-rich as a signature of $-\text{NH}_x$ ($x = 1, 2$) bonded to the g-C₃N₄ skeleton is conferred from X-ray photoelectron spectroscopy (XPS) and Fourier transform infrared (FT-IR) analyses in later sections, finally giving a stoichiometry of g-C₃N_{4.8}. Because the reaction was performed in a closed alumina crucible, the gaseous products were not all exposed to the atmosphere instantaneously. The amino groups get trapped onto the pores at the surface of carbon nitride, which leads to high nitrogen content of the sample. As a whole, ammonium carbonate modulates the nitrogen content in the carbon nitride by nitrogen infusing/ex situ doping and forms close interfacial contacts more rapidly.⁴²

The formation of phase-pure stable g-C₃N₄ from the above approach could be directly clarified by using various characterization techniques. The as-synthesized BCN and NCN samples were first characterized using powder X-ray diffraction (XRD) measurements. The wide-angle XRD patterns of BCN and NCN are compared in Figure 1a along with standard g-C₃N₄ for the crystal structure determination, where peak positions of both samples are matched well with the standard (JCPDS no. 066-0813). In both cases, the strong XRD peak at 27.8° is a characteristic interlayer stacking reflection of conjugated aromatic systems, indexed for graphitic materials as the (002) peak as shown by Ajayan and co-workers.⁴¹ However, after exfoliation the intensity of this (002) peak in the case of NCN significantly decreases and broadens, clearly demonstrating that the layered g-C₃N₄ has been successfully exfoliated from BCN. On the other hand, this peak for NCN had slightly shifted from 27.4° for BCN to 27.8°, which may be due to the reduction in correlation length of interlayer periodicity of the triazine building blocks as reported earlier.^{26,43} Furthermore, small-angle XRD (SAXS) measurement has been performed on the NCN sample to investigate the nature of the sample (inset, Figure 1a). Two well-resolved diffraction peaks are observed at 1.4° and 1.7° in the SAXS measurement, corresponding to (110) and (200) Bragg reflection planes, respectively.¹² The two well-ordered peaks clearly indicate the presence of a highly ordered mesoporous structure, which is consistent with previous reports.⁴⁴

Raman measurement has been performed in order to understand the doping effects of heteroatoms in the carbon materials and the defects present in the carbon nitride

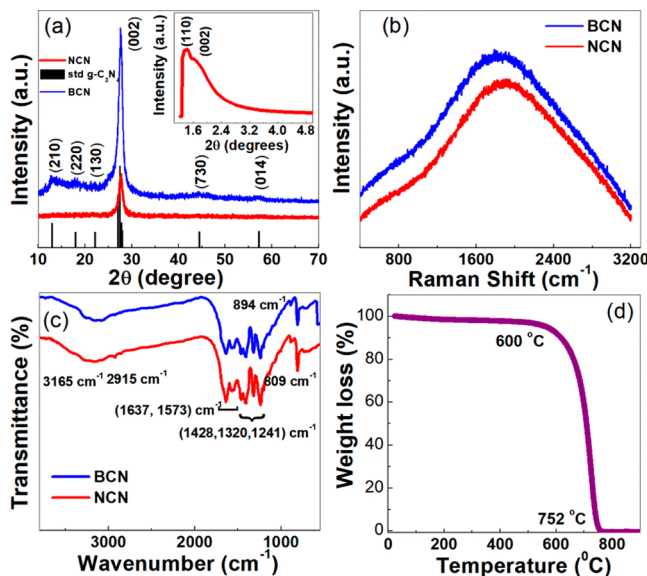


Figure 1. (a) Powder XRD pattern of as-synthesized $\text{g-C}_3\text{N}_4$ (NCN, BCN) and standard sample. (Inset) Small-angle XRD pattern of NCN. (b) Raman spectra of NCN and BCN samples. (c) Comparison of FT-IR spectra of NCN and BCN samples. (d) Thermogravimetric analysis (TGA) curve of NCN sample indicating stability of the as-synthesized sample.

structure (Figure 1b). No sharp bands are observed in the spectra; only a broad band was found at $\sim 1800 \text{ cm}^{-1}$ for both the samples, implying a defect-free structure where nitrogen atoms are perfectly incorporated into the graphitic structure of carbon material, leading to triazine structure of $\text{g-C}_3\text{N}_4$.⁷ Furthermore, to examine the surface chemical bonding state of our materials, FT-IR spectra were recorded and slightly sharper peaks for NCN sample over BCN sample were seen, corroborating enhanced absorption in the former sample (Figure 1c). The peaks for NCN sample over BCN sample can be attributed to more ordered packing of tri-*s*-triazine motifs in the nanosheets. Peaks are observed in three different major regions of the IR spectra. A sharp intense IR peak in the region of $\sim 809 \text{ cm}^{-1}$ typically corresponds to the presence of unique C–N heterocyclic framework or stems from the heptazine ring system.⁴⁵ The multiple peaks in the range of 1700 to 1200 cm^{-1} are attributed to the stretching modes of *s*-triazine derivatives. Peaks at 1428, 1320, and 1241 cm^{-1} belong to the stretching modes of C–N bonds, and those at 1573 and 1637 cm^{-1} are due to the stretching modes of C=N moieties. A sharp, small peak near 2915 cm^{-1} can be assigned to the C–H bond stretching mode of vibration. The broad peaks at 3000–3600 cm^{-1} correspond to the presence of N–H stretching of the amino groups present in the structure of $\text{g-C}_3\text{N}_4$.²⁶ Thermogravimetric analysis (TGA) clearly signifies the temperature range up to which the material can withstand without any thermal decomposition. The TGA curve of $\text{g-C}_3\text{N}_4$ obtained in the presence of static air (Figure 1d) clearly suggests that the present sample shows no thermal decomposition (weight loss) up to 600 °C and is a highly stable polymer that can endure high temperatures even in the presence of oxidizing atmosphere. The weight loss at $>600 \text{ }^\circ\text{C}$ is because of direct thermal decomposition of $\text{g-C}_3\text{N}_4$ itself, giving mainly CNH, NH₃, and C₂N₂ as decomposition products.⁶

The low-magnification TEM image (Figure 2a) clearly shows that the as-synthesized $\text{g-C}_3\text{N}_4$ has a sheetlike

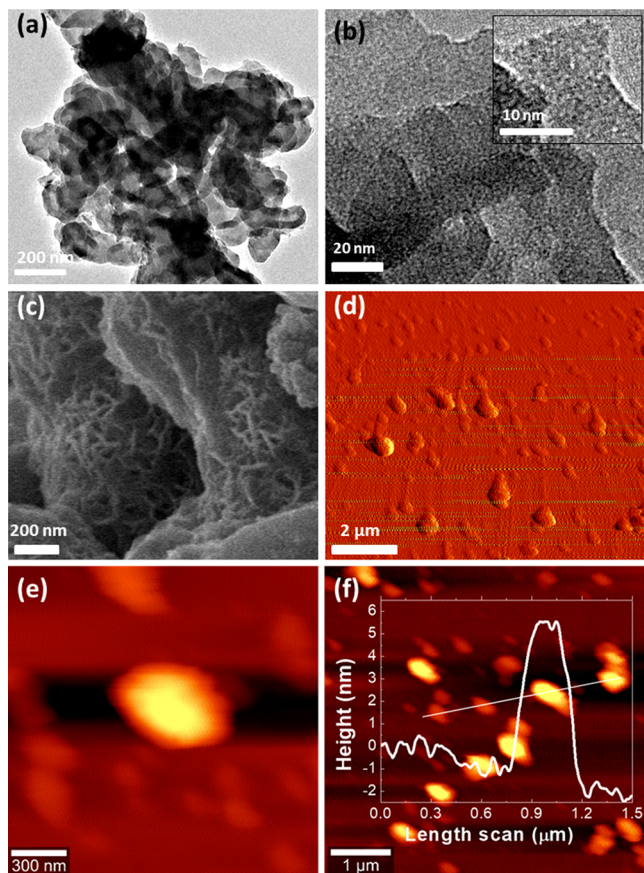


Figure 2. (a) Low-magnification transmission electron microscopy (TEM) image of as-synthesized $\text{g-C}_3\text{N}_4$ showing sheetlike morphology. (b) High-resolution TEM (HRTEM) image of single NCN holey nanosheet. (c) High-resolution field-emission scanning electron microscopy (FESEM) image. (d, e) Atomic force microscopy (AFM) images of the as-prepared NCN sample showing nanosheet topography. (f) Line scanning of a very dilute sample to measure the thickness of the sheets. (Inset) Height profile along the line.

morphology that is evident for the polymeric kind of structure of carbon nitrides. More images can be seen in Figure S2. To examine the porosity within the sheets, we have taken the HRTEM images of the sample (Figure 2b). Pores of very small size are observed on the surface of the nanosheets where the average size of the pore is found to be $\sim 2.0 \text{ nm}$ (a large HRTEM image with detectable pores is shown in Figure S3 in the Supporting Information). Both the SAXS and HRTEM measurements signify the porous (holey) structure of the as-synthesized material, which could be attributed to the enhancement in photocatalytic activity and electrochemical charge-storage activity. To further investigate the 3-dimensional morphology and surface features, FESEM imaging has been performed on the sample. A porous kind of nanosheet structure is visualized again corroborating results of SAXS and HRTEM in the high-resolution FESEM image (Figure 2c) as reported earlier.²⁰ Moreover, to elucidate the topography and the height/thickness of the as-prepared porous $\text{g-C}_3\text{N}_4$ nanosheets, we have performed AFM analyses. Figure 2d and e clearly reveals that the NCN sample has a rough surface with the typical topography of nanosheets. On performing the AFM

topological height analysis, the average height/thickness of the nanosheets was found to be in the range of 5–6 nm, as clearly seen in Figure 2f. Therefore, the thickness of the nanosheets in this range signifies that the efficient exfoliation process is needed in order to synthesize few-layer-thick g-C₃N₄ nanosheets.⁴⁶ The scanning electron microscopy–energy-dispersive X-ray spectroscopy (SEM-EDS) elemental mapping profile shows a homogeneous distribution of C and N over a large area of nanosheets for both NCN and BCN samples (Figures S4 and S5). Furthermore, FESEM-EDS and CHN analyzer methods were used to analyze the elemental ratio, which gives the final stoichiometry as C₃N_{4.8} (Figures S4e and SSg and Table S1), implying a high nitrogen content in the polymer. These additional nitrogens can be attributed to surface-adsorbed/bonded NH₃ molecules (also seen in FT-IR) formed during the decomposition of (NH₄)₂CO₃ during synthesis.

The nitrogen adsorption–desorption measurements were done in order to find out the specific Brunauer–Emmett–Teller (BET) surface area, specific pore volume, and mesoscale ordering of the as-synthesized NCN and BCN samples. Figure 3a shows a type IV isotherm exhibiting a higher multipoint

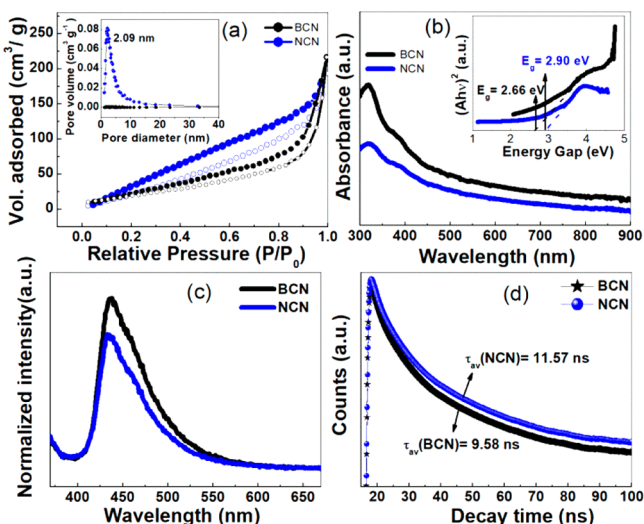


Figure 3. (a) Nitrogen adsorption–desorption isotherm at 77 K. (Inset) Barrett–Joyner–Halenda (BJH) pore-size distribution curve of NCN sample. (b) Optical absorption spectra of as-prepared NCN and bulk C₃N₄ sample dispersed in isopropyl alcohol. (Inset) Tauc's plot for the measurement of direct band gap of g-C₃N₄ samples. (c) Comparison of photoluminescence (PL) spectra of NCN and BCN. (d) Time-resolved photoluminescence (TRPL) decay profile of the NCN and BCN samples after exciting the samples at 370 nm, which shows the lower average lifetime of BCN over NCN.

BET surface area of 144 m²/g for NCN sample in comparison to BCN sample (79 m²/g). BJH adsorption pore-size distribution curve (inset of Figure 3a) revealed that NCN sample has an ordered porous structure with a pore-size diameter of 2.09 nm and specific pore volume as high as 0.377 cm³/g. Meanwhile, the pore-size distribution and pore volume are almost negligible in the case of BCN sample (inset of Figure 3a). The optical properties of NCN and BCN were studied using UV–Vis spectrophotometer, PL, and TRPL techniques at room temperature. Figure 3b shows the UV–Vis spectra of both samples, revealing properties like an intrinsic semiconductor. Two broad peaks are observed for both samples in the spectra, but the intensity of the absorption

peaks for NCN sample is slightly lower than that for the BCN sample. In both spectra, absorbance at 324 nm is due to π–π* transitions observed in conjugated ring systems and that at 410 nm is due to n–π* transitions involving lone pairs on the edge N atoms of triazine/heptazine rings.⁴⁷ Tauc's plots were further plotted in order to elucidate the direct optical band gap for both NCN sample and BCN samples (inset of Figure 3b).^{48,49} The direct band gap for the NCN sample was found to be 2.90 eV, which is higher than the band gap of BCN sample (2.64 eV). This increase in the band gap of the NCN sample is attributed to the quantum confinement effect. Because the additional N-atoms in g-C₃N_{4.8} stoichiometry are expected at the surface (bonded to *s*-triazine-based heterocycles) without disturbing the CN framework, no in situ doping is expected to lower the band gap. Transitions between the weakly localized π–π* states coming from the sp² hybridized C and N present in the CN framework contribute to the optical band gap in g-C₃N₄.⁴⁷ The formation of photoinduced charge carrier excitons, excitons separation, and their migration to the surface reaction sites are interconnected to the structural defects of semiconductor materials. To examine the separation efficiency of photogenerated electron–hole pairs and to explore the behavior of charge carriers in the samples BCN and NCN, we conducted steady-state photoluminescence (PL) measurements. All measurements were performed at room temperature with an excitation wavelength of 370 nm. PL spectra of both BCN and NCN samples are compared in Figure 3c. A weak intensity emission peak of NCN sample is observed as compared to the BCN sample, demonstrating a decrease in the recombination efficiency of charge carriers in the NCN sample. A weakened emission peak also signals toward reduced structural defects within the structure of NCN sample because defects are usually considered as sites for recombination of photogenerated electron–hole pairs.^{50–52} Therefore, to support the above points, we performed TRPL measurements to examine the decay kinetics of photogenerated charge carriers. The average lifetimes (τ_a) for the samples were calculated using eq S1. The average lifetime of radiative charge carriers for NCN sample is 11.57 ns, which is higher than the average lifetime of BCN sample (9.58 ns) as shown in Figure 3d and Table S2, implying that the increased lifetime of charge carrier in the former sample is associated with a slower recombination process. The higher lifetime of NCN sample supports the fact that there is an increase in the transfer path within the two-dimensional structure of the g-C₃N₄, which directs the free charge carriers to participate in the surface photocatalytic reaction and enhances the photocatalytic activity.²⁶

To elucidate the chemical bonding between C and N in the carbon nitride structure, XPS spectra were recorded first on the fresh sample (Figure 4a–c). Strong signals are obtained only from C and N in the survey spectrum (Figure 4a), and a weak signal is observed for O element in the XPS survey spectra as shown in Figure S6. This O 1s peak is believed to be from adsorbed oxygen on the surface of the sample. The O 1s peak (534.8 eV) was used as a reference to calibrate all the other binding energies. The deconvolution of C 1s spectra leads to three Gaussian–Lorentzian single peaks (Figure 4b). The peak at 284.5 eV corresponds to pure graphitic carbon sites (sp², C=C), the peak at 286.5 eV corresponds to N—C=N, and the peak at 288.1 eV corresponds to carbon bonded to three nitrogen atoms.^{21,25,50,53} Interestingly, three deconvoluted peaks are seen at 398.4, 400.0, and 402.0 eV, respectively,

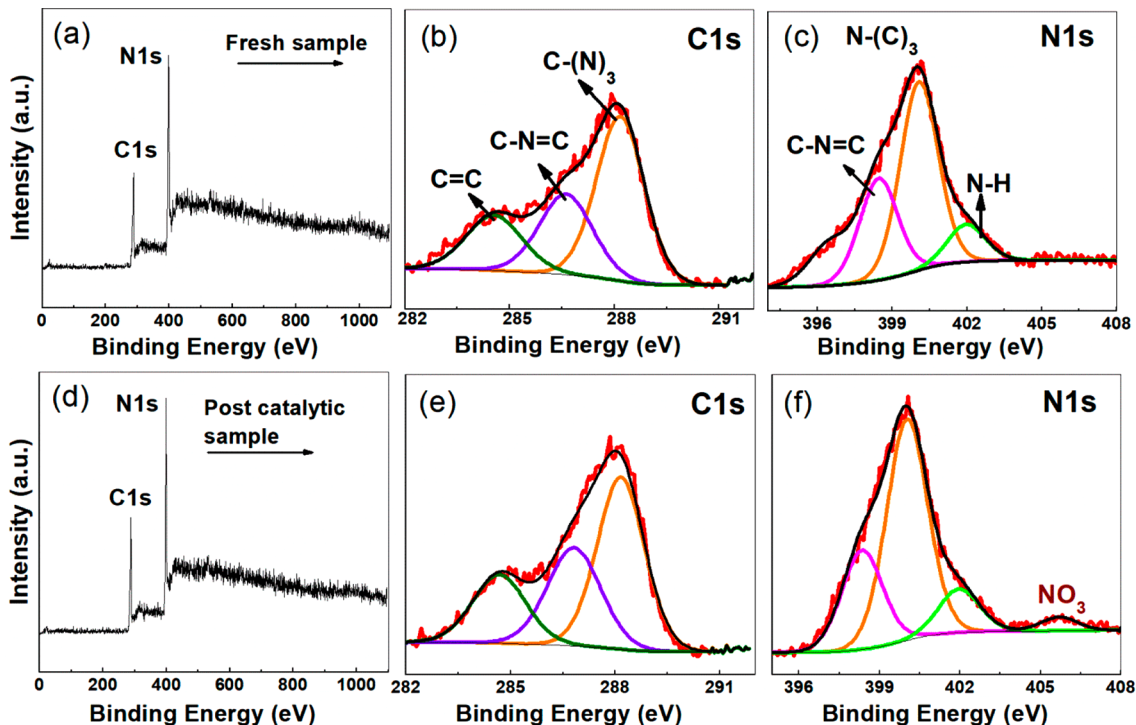


Figure 4. XPS spectra of fresh NCN sample (a–c) and postcatalytic sample (d–f). (a, d) Survey spectrum, (b, e) high-resolution XPS spectra of C 1s, and (c, f) high-resolution XPS spectra of N 1s.

during the fitting of N 1s peak. The peak at 398.4 eV corresponds to sp^2 hybridized nitrogen atom bonded to two neighboring carbon atoms, and the peak at 400.0 eV corresponds to sp^3 hybridized nitrogen atom bonded to three neighboring carbon atoms (Figure 4c).^{21,25,50,53} A peak at 402.0 eV signals the presence of ample amounts of amino groups ($-NH_x$, $x = 1, 2$),^{7,21} corroborating the results from FT-IR spectroscopy. To check the stability of the material, XPS measurements have been performed on the postphotocatalytic sample. The used catalyst sample shows similar XPS features to the fresh one with, however, a slight shift in the peak positions toward higher binding energies (Figure 4d–f). The three C 1s peaks are seen at 284.7, 286.8, and 288.2 eV, respectively, and the three N 1s peaks are observed at 398.4, 400.1, and 402.1 eV, respectively, similar to the different hybridization states as described earlier. This minor shift may be due to partial oxidation of C and N during vigorous catalytic reactions. However, chemical bondings of the material remained unchanged even after cycling for several hours signaling toward high stability of the material. A new peak that appeared at 405.8 eV in the used sample is attributed to the nitrate group,¹² which originates from the oxidation of the amine group loosely bound to the surface of the carbon nitride layer during vigorous photocatalytic water splitting reaction.

The as-synthesized g-C₃N₄ was then used in photocatalytic reduction of water to produce H₂ molecules under visible-light irradiation and was found to be very promising. At the beginning, 327 $\mu\text{mol h}^{-1} \text{g}^{-1}$ of gas mixture was evolved directly from water in the process without the use of any sacrificial agents (SAs) or cocatalysts (Figure 5a). This in fact reflects the true photocatalyst nature of our NCN nanosheets, which in turn can split water without any scavengers to form H₂ and O₂.²⁰ However, the H₂ production efficiency is practically limited by the proton reduction potential, $E^\circ(H^+/\text{H}_2) = -0.41 \text{ V}$ versus the normal hydrogen electrode (NHE) at pH 7, and also the high rate of exciton recombination. Thus, to further increase the activity, few control reactions have been carried out with three different types of widely used SA at different concentrations. Out of these SAs, maximum H₂ evolution of gas was seen in 20% triethanolamine (as obtained from GC). Optimization of catalyst loading is shown in Figure 5b. Out of various loadings, 50 mg of the catalyst was found to be the optimum amount for maximum gas evolution. Using 50

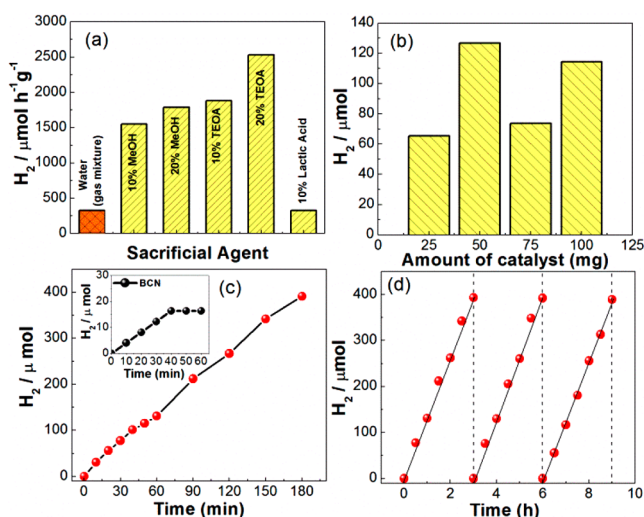
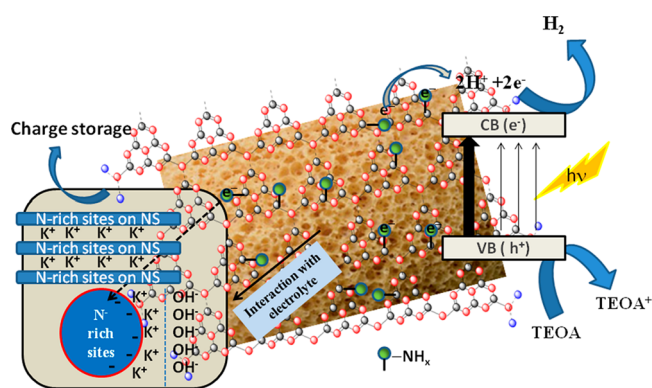


Figure 5. (a) Visible-light-driven photocatalytic H₂ evolution rate against different solution conditions using 50 mg of NCN as photocatalyst. (b) Optimization of catalyst dosage in 20% TEOA solution (1h). (c) Time course of H₂ evolution under the irradiation of visible light and in the presence of 50 mg of holey NCN NSs. (Inset) Amount of evolved H₂ using BCN as photocatalyst. (d) Recyclability study of hydrogen evolution tests with holey NCN NSs.

$H_2 = -0.41 \text{ V}$ versus the normal hydrogen electrode (NHE) at pH 7, and also the high rate of exciton recombination. Thus, to further increase the activity, few control reactions have been carried out with three different types of widely used SA at different concentrations. Out of these SAs, maximum H₂ evolution of gas was seen in 20% triethanolamine (as obtained from GC). Optimization of catalyst loading is shown in Figure 5b. Out of various loadings, 50 mg of the catalyst was found to be the optimum amount for maximum gas evolution. Using 50

mg of catalyst in the presence of 20% aqueous triethanolamine, the maximum production rate of hydrogen was observed (Figure 5c), which increases steadily with a prolonged time of light irradiation (0–3 h). After irradiation for 3 h, the average hydrogen evolution rate was found to be $2620 \mu\text{mol h}^{-1} \text{g}^{-1}$ (see Figure 5a and c). The hydrogen evolution rate of the NCN sample was 8 times higher than that of the BCN sample ($326 \mu\text{mol h}^{-1} \text{g}^{-1}$). The apparent quantum efficiency of NCN sample was calculated to be 8.5% at 427 nm, and the number of H_2 molecules produced is found to be $6.98 \times 10^{14} \text{ s}^{-1} \text{ cm}^{-1}$ (see Supporting Information for calculations). Under visible-light irradiation, our holey NCN NSs give a much higher H_2 evolution rate than the other reported $\text{g-C}_3\text{N}_4$ materials without the use of any kind of cocatalyst (Table S2). As a mechanistic view, which is not different from that reported in the literature,^{12,22,23,25,45} the porous structure with a high surface area and tunability of band positions of present NCN leads to an outstanding performance under visible-light irradiation. As the band gap is increased, the path length between the conduction band and the valence band increases, which results in suppression of recombination effect, and excitons are easily separated and move to surface reaction sites. The TRPL data already indicated a longer average lifetime of charge carriers in the case of NCN sample. Then the holes are effectively scavenged by the SA used, and hence, electrons are finally used in the reduction of water to give H_2 .⁴ At the same time, the presence of loosely bound $-\text{NH}_x$ groups at the surface of nanosheets and, hence, the free electron lone pairs also effectively and additionally contributed to the reduction of H^+ to H_2 , because $-\text{NH}_x$ is an electron-donating group. A schematic mechanism of the photocatalytic process and proposed electron donation from $-\text{NH}_x$ groups to the reduction of H^+ is shown in Scheme 2. It is reported that

Scheme 2. Schematic Diagram of Mechanisms Showing the Evolution of H_2 (Right Side) and EDLC Capacitance (Left Side) by Stand-Alone N-Rich Holey NCN Nanosheets^a



^aBand gap excited electrons as well as electrons donated by $-\text{NH}_x$ groups effectively reduce H^+ during the catalytic reaction to H_2 gas. Porous structure as well as easy intercalation of K^+ due to the presence of N-rich sites on $\text{g-C}_3\text{N}_4$ nanosheets effectively induces high EDLC-type capacitance.

the electronic band structure of NH_3 molecule adsorbed (ex situ doping) on a host material yields *n*-type doping, pinning the Fermi level near the conduction band (CB) of the host material, such as Si nanowires.⁵⁴ Similar investigation on $-\text{NH}_x$ group is unavailable, but based on electronic structure of liquid ammonia⁵⁵ and band structure of $\text{g-C}_3\text{N}_4$ ^{16–18} as well

as on our experimental studies, it is clear that CB and Fermi level of $-\text{NH}_x$ is more negative than CB of $\text{g-C}_3\text{N}_4$. Thus, the abundant $-\text{NH}_x$ anchoring at the surface of $\text{g-C}_3\text{N}_4$ in the present case also acts as a shallow donor and may donate electrons to the CB of the carbon nitride. However, instead of recombination with holes (low-intensity emission peak, Figure 3c), these electrons stay at the surface for a longer time (high average lifetime, Figure 3d) and take part effectively in hydrogen reduction reaction in solution.

In addition to postcatalytic XPS studies (Figure 4d–f), we have performed XRD and TEM measurements on the used samples. No difference in XRD peak positions and intensity was observed between the fresh and used catalyst (Figure S7a). Moreover, no new XRD peak appeared in the XRD pattern of the used sample. TEM imaging of used samples (Figure S7b and c) also justify retention of porous sheetlike morphology of used sample. Thus, from XPS, XRD, and TEM analyses, it is found that the used sample after 9 h of vigorous photocatalytic reactions remained stable with structure, morphology, and composition. Hence, our NCN catalyst can be used for prolonged photocatalytic water splitting cycles without any destruction of its structure.

Charge-Storage Behavior. Because of the graphene-like structure, high surface area, holey topography, and possession of higher concentration of surface nitrogen, which is favorable for higher conductivity and electrochemical performance,^{29–31} we chose to first investigate the charge-storage characteristics of NCN and BCN materials using a conventional three-electrode-based configuration, and the results are compared in Figure S8. To examine the initial electrochemical performances, such as electronic conductivity and capacitive behavior of three-electrode cell based on NCN and BCN, impedance spectrum (Nyquist plot) was measured in the frequency range 10 MHz–100 kHz using 1.0 M KOH electrolyte (Figure S8a and d). A steep rise in the impedance response (Z'') at the lower-frequency region clearly indicates characteristics approaching the ideal capacitive behavior. Bulk resistance (R_b), electrode–electrolyte charge-transfer resistance (R_{ct}), and bulk properties of the cells are calculated from the expanded weak semicircular arc part of the Nyquist plot at higher-frequency region (insets of Figure S8a and b). The calculated R_b , R_{ct} , and total resistance ($R_b + R_{ct}$) of Cell#NCN are found to be as small as 2.02, 2.18, and $4.20 \Omega \text{ cm}^2$, respectively, implying more conducting nature of the NCN material compared to the BCN material. This high conductivity can be corroborated to high nitrogen atom content of the present $\text{g-C}_3\text{N}_4$ NS materials as proved from CHN and EDS measurements. Cyclic voltammetry (CV) profiles of both cells were recorded in a potential window ranging from –0.2 to 0.3 V at various scan rates from 20 to 100 mV s^{–1} (Figure S8b and e). Typical semirectangular-shaped voltammograms without redox peaks are observed, indicating a complete EDLC behavior. However, very high area as acquired by Cell#NCN over Cell#BCN signified a higher specific capacitance of the former, which was also further confirmed by GCD measurements. In addition to semirectangular CV patterns, both samples also possess triangular-shaped GCD curves (without any plateau), depicting an electrical double layer capacitor behavior with good electrochemical reversibility and Coulombic efficiency (Figure S8c and f). Interesting differences in electrochemical charge storage between NCN and BCN cells are observed during these courses of GCD measurements. While the maximum charging current could reach 5 mA (or 8.3 Ag^{-1} current

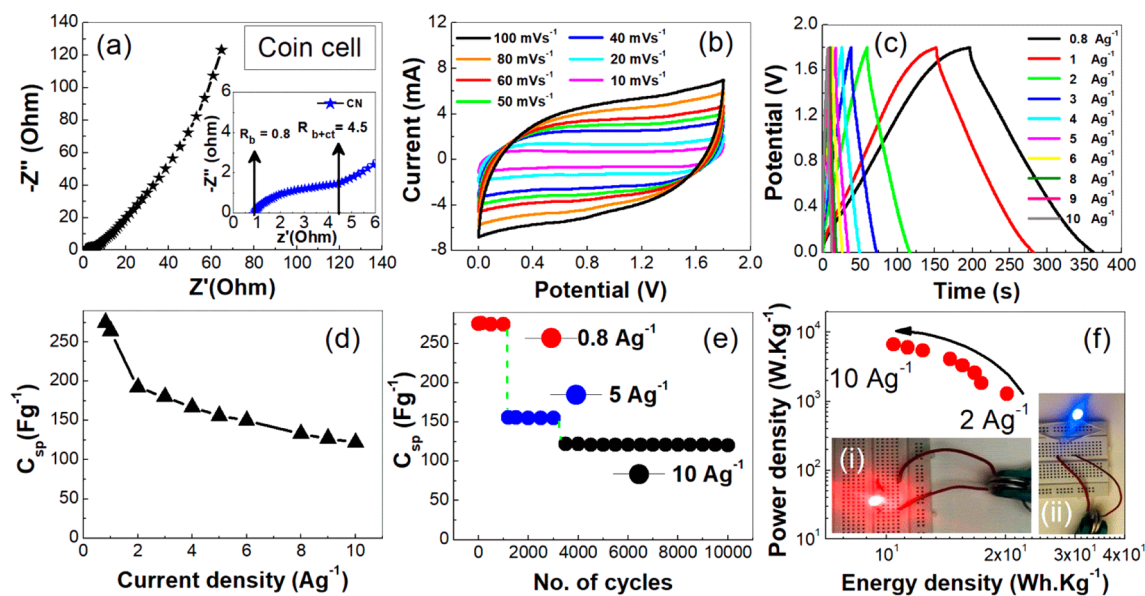


Figure 6. (a) EIS plot of NCN coin cell recorded at room temperature in the frequency range from 10 mHz to 100 kHz. (Inset) Expanded representations of the impedance plots in the high-frequency region to analyze R_b and R_{ct} values. (b) Cyclic voltammograms of the capacitor NCN coin cell at different scan rates using 6.0 M KOH electrolyte. (c) Comparison of GCD cycles at different current densities. (d) Comparison of the specific capacitance at different current densities ($0.8\text{--}10\text{ Ag}^{-1}$). (e) Plot of specific capacitance versus number of cycles up to 10 000 cycles at the indicated current densities. (f) Ragone plot of the NCN supercapacitor cell. The energy density and power density were calculated from the charge–discharge curves at various current densities. (Inset i, ii) Photographs of red and blue LEDs lighted by two series-connected supercapacitors, where the coin cells are charged at a 1.8 V potential window.

density) in the case of Cell#NCN, Cell#BCN can be charged up to a maximum 0.22 mA (or 0.37 Ag^{-1} , as seen from CV profile) only. In addition, Cell#NCN electrode possesses a high specific capacitance (C_{sp}) value of 94, 90, 87, 86, 83, 80, 78, 76, and 73 F g^{-1} at a current of 0.8, 1.0, 1.5, 2.0, 2.5, 3.0, 3.5, 4.0, and 5.0 mA , respectively. However, the maximum C_{sp} obtained for Cell#BCN is only 7.4 F g^{-1} at a current of 0.12 mA, implying the superiority of nanosheet material over the bulk sample.

Encouraged by the above-mentioned fascinating and novel charge-storage behavior of the present ultrathin holey g-C₃N_{4.8} nanosheet electrode as compared to the bulk counterpart, we have opted to make a coin cell device composed of the same material as the working electrode. Coin cells are widely recognized as the standard test platform for supercapacitor and lithium ion battery electrode research. To study the electrochemical performances of the coin cell device, we have performed various initial studies similar to the three-electrode configuration. The impedance spectrum (Nyquist plot) in Figure 6a shows a total resistance of $4.5\Omega\text{ cm}^2$, which is almost similar to that of Cell#NCN in the three-electrode system. To rate the performance of the device, CV and GCD studies were done, and the results are shown in Figure 6b and c. The CV profiles were recorded in a potential window ranging from 0 to 1.8 V at various scan rates from 10 to 100 mV s⁻¹. The semirectangular-shaped voltammograms acquired high surface area and no redox peaks, signifying true EDLC behavior. The GCD curves of the NCN coin cell were triangular-shaped without any plateau, representing again an EDLC behavior with good electrochemical reversibility and Coulombic efficiency. Figure 6c shows a comparison of the single charge–discharge cycles for the coin cell at different current densities ($0.8\text{--}10\text{ Ag}^{-1}$) charged in the range of 0.0–1.8 V. A crucial parameter for a good supercapacitor is the high discharging duration of the material, which is quite high in the

present case, as clearly seen in the GCD curves. The device delivers discharge-specific high capacitance (C_{sp}) as high as 275, 264, 192, 180, 167, 156, 150, 133, 127, and 122 F g^{-1} at an applied current density of 0.8, 1.0, 2.0, 3.0, 4.0, 5.0, 6.0, 8.0, 9.0, and 10.0 A g^{-1} , respectively. Figure 6d shows values of C_{sp} at different applied current densities, where C_{sp} decreased gradually with increasing current, entailing a high rate capability of present g-C₃N₄ NS-based electrode (Table 1).

Table 1. Calculated Values of C_{sp} , E , and P for Cell#NCN at Respective Applied Current Density

current density (A g ⁻¹)	C_{sp} (F g ⁻¹)	energy density (Wh kg ⁻¹)	power density (W kg ⁻¹)
0.8	275	30	655
1	264	28	782
2	192	20	1270
3	180	17	1830
4	167	16	2607
5	156	15	3314
6	150	14	4073
8	133	12	5439
9	127	11	6021
10	122	10	6651

A higher C_{sp} value at lower current density or vice versa is observed, which is due to the accessible maximum surface area of the material for the diffusion of ions from the electrolyte. At higher current density, the effective interaction between the ions and the electrode is reduced, resulting in a reduction in capacitance.⁵⁶ The high specific capacitance value of the material (without the use of Ni foam as substrate) can be attributed to the following reasons: (i) the high electrical conductivity arises due to the extended delocalized π -electrons of the tri-s-triazine structure of the g-C₃N₄³⁵ as well as the

presence of free electron lone pair on surface-adsorbed N atoms (**Scheme 2**), and (ii) large surface area and a highly porous structure of the material allow the storage of charges by adsorption/desorption of ions in an electric double layer formed at the interface of electrolyte and electrode (**Scheme 2**, intercalation mechanism).⁵⁷

Good cycling stability with capacitance retention is another important deliverable of this NCN-based coin cell device. To examine the potential of the active material as working electrode for practical applications, cycling stability test was performed. **Figure 6e** displays the electrochemical cycling stability of NCN coin cell when we increase current density from 0.8 to 10.0 A g^{-1} for 10 000 GCD cycles. It can be found that the active electrode material retained >98% of its initial specific capacitance at different current densities until the measured 10 000 cycles, clearly indicating a good cycling stability. A good cycling stability is due to the porous structure of the as-synthesized $\text{g-C}_3\text{N}_4$ nanosheets, leading to faster diffusion of ions between the electrode and electrolyte interface.⁵⁸ The obtained capacitance and stability values of the present study are compared with the available $\text{g-C}_3\text{N}_4$ literature in **Table S3**. The energy densities (*E*) and power densities (*P*) of NCN coin cell were determined using **eqs 4** and **5** and are recorded in **Table 1**. The Ragone plot of the coin cell device is illustrated in **Figure 6f** only for applied current density of 2.0–10.0 A g^{-1} . The plot is in close agreement to the previously reported various electrical energy-storage devices based on $\text{g-C}_3\text{N}_4$ material.^{30,59} The obtained energy density is 30 Wh kg^{-1} and the power density is 655 W kg^{-1} at 0.8 A g^{-1} , where the power density can be increased to 6651 W kg^{-1} by increasing the applied current density to 10.0 A g^{-1} . These results indicate that the supercapacitor based on the nanosheet material can operate with high energy and power densities. To demonstrate this, two of our as-assembled $\text{g-C}_3\text{N}_{4.8}$ supercapacitor coin cell test devices (charged at 1.8 V) are connected in series that are capable of lighting red or blue LEDs for several min (inset **Figure 6f**), indicating their high energy storage.

CONCLUSIONS

In summary, ultrathin holey $\text{g-C}_3\text{N}_{4.8}$ nanosheets have been synthesized using commonly available and cheap feedstocks via direct thermal polymerization method. The as-synthesized material has been characterized by various advanced techniques such as powder XRD, HRTEM, FESEM, XPS, BET, Raman, FT-IR, and various other techniques. It shows an excellent photocatalytic hydrogen evolution activity (2620 $\mu\text{mol h}^{-1} \text{g}^{-1}$) from water under visible-light irradiation and a prominent apparent quantum yield of 8.5% at 427 nm in the absence of any kind of cocatalyst as compared to the previous reports and long recycling stability. Moreover, the material is found to show EDLC-type charge-storage behavior with high specific capacitance (275 F g^{-1} at 0.8 A g^{-1}) and great cycling stability. The power density reaches as high as 6651 W kg^{-1} , similar to an EDLC cell with an energy density of 10 Wh kg^{-1} . The enhancement in these activities and sustainability can be correlated to several factors, such as (i) high accessible specific surface area due to the presence of the pores on the surface of 2D nanosheets. This gives a higher number of active sites needed for the photocatalytic hydrogen evolution as well as effective interaction of electrolyte ions with the interior part of present $\text{g-C}_3\text{N}_4$ during charge-storage activity. (ii) Delocalization of π -electrons within the 2D NCN structure increases the

electrical conductivity within the nanosheets. (iii) The high average lifetime of charge carrier also enhances photocatalytic efficiency. (iv) The presence of high nitrogen contents (free lone pairs of electrons) at the surface generates more basic sites. The basic sites can efficaciously interact with both OH^- ions during charge storing and provide additional electrons during photocatalytic hydrogen evolution.

ASSOCIATED CONTENT

Supporting Information

The Supporting Information is available free of charge on the ACS Publications website at DOI: [10.1021/acssuschemeng.9b00626](https://doi.org/10.1021/acssuschemeng.9b00626).

Materials; characterization techniques; calculation on average lifetime; calculations of Donor concentration, number of H_2 molecule produced, and apparent quantum efficiency; TEM/HRTEM/FESEM/EDS images of different samples, CHN analysis, O 1s XPS, activity comparison table, postcatalytic sample characterization, EIS, CV, and GCD ([PDF](#))

AUTHOR INFORMATION

Corresponding Author

*E-mail: sdeka@chemistry.du.ac.in, ssdeka@gmail.com.

ORCID

C. S. Gopinath: [0000-0002-4525-3912](https://orcid.org/0000-0002-4525-3912)

Sasanka Deka: [0000-0003-4794-0406](https://orcid.org/0000-0003-4794-0406)

Notes

The authors declare no competing financial interest.

ACKNOWLEDGMENTS

B.A. and L.K. thank CSIR-India and UGC-India, respectively, for providing research fellowships. S.D. gratefully acknowledges the financial support received from DST-SERB-New Delhi (EMR/2016/004833). The authors thank USIC-DU and SAIF-AIIMS facilities for sample characterizations and IISER-Mohali for SAXS and JNU-AIRF for AFM measurements.

REFERENCES

- (1) Wang, X.; Maeda, K.; Thomas, A.; Takanabe, K.; Xin, G.; Carlsson, J.; Domen, K.; Antonietti, M. A. Metal-Free Polymeric Photocatalyst for Hydrogen Production from Water under Visible Light. *Nat. Mater.* **2009**, *8*, 76–80.
- (2) Wang, X.; Maeda, K.; Chen, X.; Takanabe, K.; Domen, K.; Hou, Y.; Fu, X.; Antonietti, M. Polymer Semiconductors for Artificial Photosynthesis: Hydrogen Evolution by Mesoporous Graphitic Carbon Nitride with Visible Light. *J. Am. Chem. Soc.* **2009**, *131*, 1680–1681.
- (3) Maeda, K.; Wang, X.; Nishihara, Y.; Lu, D.; Antonietti, M.; Domen, K. Photocatalytic Activities of Graphitic Carbon Nitride Powder for Water Reduction and Oxidation under Visible Light. *J. Phys. Chem. C* **2009**, *113*, 4940–4947.
- (4) Wang, X.; Blechert, S.; Antonietti, M. Polymeric Graphitic Carbon Nitride for Heterogeneous Photocatalysis. *ACS Catal.* **2012**, *2*, 1596–1606.
- (5) Xu, J.; Wang, Y.; Zhu, Y. Nanoporous Graphitic Carbon Nitride with Enhanced Photocatalytic Performance. *Langmuir* **2013**, *29*, 10566–10572.
- (6) Zhu, J.; Xiao, P.; Li, H.; Carabineiro, S. Graphitic Carbon Nitride: Synthesis, Properties, and Applications in Catalysis. *ACS Appl. Mater. Interfaces* **2014**, *6*, 16449–16465.

- (7) Hou, Y.; Yang, J.; Lei, C.; Yang, B.; Li, Z.; Xie, Y.; Zhang, X.; Lei, L.; Chen, J. Nitrogen Vacancy Structure Driven Photoelectrocatalytic Degradation of 4-Chlorophenol using Porous Graphitic Carbon Nitride Nanosheets. *ACS Sustainable Chem. Eng.* **2018**, *6*, 6497–6506.
- (8) Patnaik, S.; Martha, S.; Parida, K. An Overview of the Structural, Textural and Morphological Modulations of $\text{g-C}_3\text{N}_4$ towards Photocatalytic Hydrogen Production. *RSC Adv.* **2016**, *6*, 46929–46951.
- (9) Lakhi, K.; Park, D.; Al-Bahily, K.; Cha, W.; Viswanathan, B.; Choy, J.; Vinu, A. Mesoporous Carbon Nitrides: Synthesis, Functionalization, and Applications. *Chem. Soc. Rev.* **2017**, *46*, 72–101.
- (10) Yan, H. Soft-Templating Synthesis of Mesoporous Graphitic Carbon Nitride with Enhanced Photocatalytic H_2 Evolution under Visible Light. *Chem. Commun.* **2012**, *48*, 3430–3432.
- (11) Zhang, G.; Zhang, J.; Zhang, M.; Wang, X. Polycondensation of Thiourea into Carbon Nitride Semiconductors as visible Light Photocatalysts. *J. Mater. Chem.* **2012**, *22*, 8083.
- (12) Zhao, Z.; Dai, Y.; Lin, J.; Wang, G. Highly-Ordered Mesoporous Carbon Nitride with Ultrahigh Surface Area and Pore Volume as a Superior Dehydrogenation Catalyst. *Chem. Mater.* **2014**, *26*, 3151–3161.
- (13) Lin, J.; Pan, Z.; Wang, X. Photochemical Reduction of CO_2 by Graphitic Carbon Nitride Polymers. *ACS Sustainable Chem. Eng.* **2014**, *2*, 353–358.
- (14) Zhao, Z.; Sun, Y.; Dong, F. Graphitic Carbon Nitride based Nanocomposites: A Review. *Nanoscale* **2015**, *7*, 15–37.
- (15) Shen, M.; Zhang, L.; Shi, J. Converting CO_2 into fuels by graphitic carbon nitride-based photocatalysts. *Nanotechnology* **2018**, *29*, 412001.
- (16) Zhang, S.; Gu, P.; Ma, R.; Luo, C.; Wen, T.; Zhao, G.; Cheng, W.; Wang, X. Recent Developments in Fabrication and Structure Regulation of Visible-Light-Driven $\text{g-C}_3\text{N}_4$ -Based Photocatalysts towards Water Purification: A Critical Review. *Catal. Today* **2018**, DOI: 10.1016/j.cattod.2018.09.013.
- (17) Zhang, S.; Song, S.; Gu, P.; Ma, R.; Wei, D.; Zhao, G.; Wen, T.; Jehan, R.; Hu, B.; Wang, X. Visible-Light-Driven Activation of Persulfate Over Cyano and Hydroxyl Group Co-Modified Mesoporous $\text{g-C}_3\text{N}_4$ For Boosting Bisphenol A Degradation. *J. Mater. Chem. A* **2019**, *7*, 5552–5560.
- (18) Zhang, S.; Liu, Y.; Gu, P.; Ma, R.; Wen, T.; Zhao, G.; Li, L.; Ai, Y.; Hu, C.; Wang, X. Enhanced Photodegradation of Toxic Organic Pollutants Using Dual-Oxygen-Doped Porous $\text{g-C}_3\text{N}_4$: Mechanism Exploration from both Experimental and DFT Studies. *Appl. Catal., B* **2019**, *248*, 1–10.
- (19) Kudo, A.; Miseki, Y. Heterogeneous Photocatalyst Materials for Water Splitting. *Chem. Soc. Rev.* **2009**, *38*, 253–278.
- (20) Zhang, Y.; Liu, J.; Wu, G.; Chen, W. Porous Graphitic Carbon Nitride synthesized via Direct Polymerization of Urea for Efficient Sunlight-Driven Photocatalytic Hydrogen Production. *Nanoscale* **2012**, *4*, 5300–5303.
- (21) Han, Q.; Cheng, Z.; Wang, B.; Zhang, H.; Qu, L. Significant Enhancement of Visible-Light-Driven Hydrogen Evolution by Structure Regulation of Carbon Nitrides. *ACS Nano* **2018**, *12*, 5221–5227.
- (22) Mane, G.; Talapaneni, S.; Lakhi, K.; Ilbeygi, H.; Ravon, U.; Al-Bahily, K.; Mori, T.; Park, D.; Vinu, A. Highly Ordered Nitrogen-Rich Mesoporous Carbon Nitrides and Their Superior Performance for Sensing and Photocatalytic Hydrogen Generation. *Angew. Chem., Int. Ed.* **2017**, *56*, 8481–8485.
- (23) Talapaneni, S.; Mane, G.; Park, D.; Lakhi, K.; Ramadass, K.; Joseph, S.; Skinner, W.; Ravon, U.; Al-Bahily, K.; Vinu, A. Diaminotetrazine based Mesoporous C_3N_6 with a Well-Ordered 3D Cubic Structure and its Excellent Photocatalytic Performance for Hydrogen Evolution. *J. Mater. Chem. A* **2017**, *5*, 18183–18192.
- (24) Lau, V.; Yu, V.; Ehrat, F.; Botari, T.; Moudrakovski, I.; Simon, T.; Duppel, V.; Medina, E.; Stolarczyk, J.; Feldmann, J.; et al. et al. Urea-Modified Carbon Nitrides: Enhancing Photocatalytic Hydrogen Evolution by Rational Defect Engineering. *Adv. Energy Mater.* **2017**, *7*, 1602251.
- (25) Cui, L.; Song, J.; McGuire, A.; Kang, S.; Fang, X.; Wang, J.; Yin, C.; Li, X.; Wang, Y.; Cui, B. Constructing Highly Uniform Onion-Ring-Like Graphitic Carbon Nitride for Efficient Visible-Light-Driven Photocatalytic Hydrogen Evolution. *ACS Nano* **2018**, *12*, 5551–5558.
- (26) Fang, Z.; Hong, Y.; Li, D.; Luo, B.; Mao, B.; Shi, W. One-Step Nickel Foam Assisted Synthesis of Holey $\text{g-C}_3\text{N}_4$ Nanosheets for Efficient Visible-Light Photocatalytic H_2 Evolution. *ACS Appl. Mater. Interfaces* **2018**, *10*, 20521–20529.
- (27) Devaraji, P.; Gopinath, C. Pt – $\text{g-C}_3\text{N}_4$ – (Au/TiO_2): Electronically Integrated Nanocomposite for Solar Hydrogen Generation. *Int. J. Hydrogen Energy* **2018**, *43*, 601–613.
- (28) Xia, P.; Liu, M.; Cheng, B.; Yu, J.; Zhang, L. Dopamine Modified $\text{g-C}_3\text{N}_4$ and Its Enhanced Visible-Light Photocatalytic H_2 -Production Activity. *ACS Sustainable Chem. Eng.* **2018**, *6*, 8945–8953.
- (29) Tahir, M.; Cao, C.; Butt, F.; Idrees, F.; Mahmood, N.; Ali, Z.; Aslam, I.; Tanveer, M.; Rizwan, M.; Mahmood, T. Tubular Graphitic- C_3N_4 : A Prospective Material for Energy Storage and Green Photocatalysis. *J. Mater. Chem. A* **2013**, *1*, 13949–13955.
- (30) Tahir, M.; Cao, C.; Mahmood, N.; Butt, F.; Mahmood, A.; Idrees, F.; Hussain, S.; Tanveer, M.; Ali, Z.; Aslam, I. Multifunctional $\text{g-C}_3\text{N}_4$ Nanofibers: A Template-Free Fabrication and Enhanced Optical, Electrochemical, and Photocatalyst Properties. *ACS Appl. Mater. Interfaces* **2014**, *6*, 1258–1265.
- (31) Lin, R.; Li, Z.; Abou El Amaiem, D.; Zhang, B.; Brett, D.; He, G.; Parkin, I. A. General Method for Boosting the Supercapacitor Performance of Graphitic Carbon Nitride/Graphene Hybrids. *J. Mater. Chem. A* **2017**, *5*, 25545–25554.
- (32) Wei, B.; Liang, H.; Wang, R.; Zhang, D.; Qi, Z.; Wang, Z. One-Step Synthesis of Graphitic- $\text{C}_3\text{N}_4/\text{ZnS}$ Composites for Enhanced Supercapacitor Performance. *J. Energy Chem.* **2018**, *27*, 472–477.
- (33) Hao, L.; Li, X.; Zhi, L. Carbonaceous Electrode Materials for Supercapacitors. *Adv. Mater.* **2013**, *25*, 3899–3904.
- (34) Iro, Z. S.; Subramani, C.; Dash, S. S. A Brief Review on Electrode Materials for Supercapacitor. *Int. J. Electrochem. Sci.* **2016**, 10628–10643.
- (35) Zhao, L.; Fan, L.; Zhou, M.; Guan, H.; Qiao, S.; Antonietti, M.; Titirici, M. Nitrogen-Containing Hydrothermal Carbons with Superior Performance in Supercapacitors. *Adv. Mater.* **2010**, *22*, S202–S206.
- (36) Bag, S.; Roy, K.; Gopinath, C.; Raj, C. Facile Single-Step Synthesis of Nitrogen-Doped Reduced Graphene Oxide- Mn_3O_4 Hybrid Functional Material for the Electrocatalytic Reduction of Oxygen. *ACS Appl. Mater. Interfaces* **2014**, *6*, 2692–2699.
- (37) Chauhan, M.; Soni, K.; Karthik, P. E.; Reddy, K. P.; Gopinath, C. S.; Deka, S. Promising Visible-Light Driven Hydrogen Production from Water on a Highly Efficient CuCo_2S_4 Nanosheet Photocatalyst. *J. Mater. Chem. A* **2019**, *7*, 6985–6994.
- (38) Melvin, A. A.; Illath, K.; Das, T.; Raja, T.; Bhattacharyya, S.; Gopinath, C. S. M– Au/TiO_2 (M = Ag, Pd, and Pt) Nanophotocatalyst for Overall Solar Water Splitting: Role of Interfaces. *Nanoscale* **2015**, *7*, 13477–13488.
- (39) Deori, K.; Ujjain, S.; Sharma, R.; Deka, S. Morphology Controlled Synthesis of Nanoporous Co_3O_4 Nanostructures and their Charge Storage Characteristics in Supercapacitors. *ACS Appl. Mater. Interfaces* **2013**, *5*, 10665–10672.
- (40) Chauhan, H.; Singh, M. K.; Kumar, P.; Hashmi, S. A.; Deka, S. Development of SnS_2/RGO Nanosheet Composite for Cost-Effective Aqueous Hybrid Supercapacitors. *Nanotechnology* **2017**, *28*, 025401.
- (41) Yang, S.; Gong, Y.; Zhang, J.; Zhan, L.; Ma, L.; Fang, Z.; Vajtai, R.; Wang, X.; Ajayan, P. Exfoliated Graphitic Carbon Nitride Nanosheets as Efficient Catalysts for Hydrogen Evolution under Visible Light. *Adv. Mater.* **2013**, *25*, 2452–2456.
- (42) Han, Q.; Wang, B.; Gao, J.; Qu, L. Graphitic Carbon Nitride/Nitrogen-Rich Carbon Nanofibers: Highly Efficient Photocatalytic Hydrogen Evolution Without Cocatalysts. *Angew. Chem., Int. Ed.* **2016**, *55*, 10849–10853.

- (43) Liang, Q.; Li, Z.; Yu, X.; Huang, Z.; Kang, F.; Yang, Q. Macroscopic 3D Porous Graphitic Carbon Nitride Monolith for enhanced Photocatalytic Hydrogen Evolution. *Adv. Mater.* **2015**, *27*, 4634–4639.
- (44) Vinu, A. Two-Dimensional Hexagonally-Ordered Mesoporous Carbon Nitrides with Tunable Pore Diameter, Surface Area and Nitrogen Content. *Adv. Funct. Mater.* **2008**, *18*, 816–827.
- (45) Fang, L.; Li, Y.; Liu, P.; Wang, D.; Zeng, H.; Wang, X.; Yang, H. Facile Fabrication of Large-Aspect-Ratio g-C₃N₄ Nanosheets for Enhanced Photocatalytic Hydrogen Evolution. *ACS Sustainable Chem. Eng.* **2017**, *5*, 2039–2043.
- (46) Liu, M.; Xia, P.; Zhang, L.; Cheng, B.; Yu, J. Enhanced Photocatalytic H₂-Production Activity of g-C₃N₄ Nanosheets via Optimal Photodeposition of Pt as Cocatalyst. *ACS Sustainable Chem. Eng.* **2018**, *6*, 10472–10480.
- (47) Jorge, A.; Martin, D.; Dhanoa, M.; Rahman, A.; Makwana, N.; Tang, J.; Sella, A.; Corà, F.; Firth, S.; Darr, J.; et al. H₂ and O₂ Evolution from Water Half-Splitting Reactions by Graphitic Carbon Nitride Materials. *J. Phys. Chem. C* **2013**, *117*, 7178–7185.
- (48) Tauc, J. Optical properties and electronic structure of amorphous Ge and Si. *Mater. Res. Bull.* **1968**, *3*, 37–46.
- (49) Kush, P.; Ujjain, S.; Mehra, N.; Jha, P.; Sharma, R.; Deka, S. Development and Properties of Surfactant-Free Water-Dispersible Cu₂ZnSnS₄ nanocrystals: A Material for Low-Cost Photovoltaics. *ChemPhysChem* **2013**, *14*, 2793–2799.
- (50) Elbanna, O.; Fujitsuka, M.; Majima, T. g-C₃N₄/TiO₂ Mesocrystals Composite for H₂ evolution under Visible-Light Irradiation and Its Charge Carrier Dynamics. *ACS Appl. Mater. Interfaces* **2017**, *9*, 34844–34854.
- (51) Xing, W.; Tu, W.; Han, Z.; Hu, Y.; Meng, Q.; Chen, G. Template-Induced High-Crystalline g-C₃N₄ Nanosheets for Enhanced Photocatalytic H₂ Evolution. *ACS Energy Lett.* **2018**, *3*, 514–519.
- (52) Chauhan, H.; Kumar, Y.; Dana, J.; Satpati, B.; Ghosh, H. N.; Deka, S. Photoinduced ultrafast charge separation in colloidal 2-dimensional CdSe/CdS-Au hybrid nanoplatelets and corresponding application in photocatalysis. *Nanoscale* **2016**, *8*, 15802–15812.
- (53) Lin, Q.; Li, L.; Liang, S.; Liu, M.; Bi, J.; Wu, L. Efficient Synthesis of Monolayer Carbon Nitride 2D Nanosheet with Tunable Concentration and enhanced Visible-Light Photocatalytic Activities. *Appl. Catal., B* **2015**, *163*, 135–142.
- (54) Miranda, Á.; Cartoixà, X.; Canadell, E.; Rurali, R. NH₃ Molecular Doping of Silicon Nanowires Grown Along the [112], [110], [001], and [111] Orientations. *Nanoscale Res. Lett.* **2012**, *7*, 308.
- (55) Vogler, T.; Vöhringer, P. Probing The Band Gap of Liquid Ammonia with Femtosecond Multiphoton Ionization Spectroscopy. *Phys. Chem. Chem. Phys.* **2018**, *20*, 25657–25665.
- (56) Chen, Q.; Zhao, Y.; Huang, X.; Chen, N.; Qu, L. Three-Dimensional Graphitic Carbon Nitride Functionalized Graphene-Based High-Performance Supercapacitors. *J. Mater. Chem. A* **2015**, *3*, 6761–6766.
- (57) Wang, Y.; Song, Y.; Xia, Y. Electrochemical Capacitors: Mechanism, Materials, Systems, Characterization and Applications. *Chem. Soc. Rev.* **2016**, *45*, 5925–5950.
- (58) Kumar, L.; Chauhan, H.; Yadav, N.; Yadav, N.; Hashmi, S.; Deka, S. Faster Ion Switching NiCo₂O₄ Nanoparticle Electrode-Based Supercapacitor Device with High Performances and Long Cycling Stability. *ACS Appl. Energy Mater.* **2018**, *1*, 6999–7006.
- (59) Chen, Q.; Zhao, Y.; Huang, X.; Chen, N.; Qu, L. Three-Dimensional Graphitic Carbon Nitride Functionalized Graphene-Based High-Performance Supercapacitors. *J. Mater. Chem. A* **2015**, *3*, 6761–6766.